

Journal of Seismic Exploration

ARTICLE

Forward modeling study of seismic acquisition for fractured soft structures in deep geothermal reservoirs

Guoqiang Fu¹, Zhiyu Tan¹, Zhe Men², Fei Gong³, Ping Che⁴, Qiang Guo¹, Xiaoge Wu¹, Fan Xiao¹, and Jingyi Lei¹

¹Department of Geophysics, School of Resources and Geosciences, China University of Mining and Technology, Xuzhou, Jiangsu, China

²China National Petroleum Corporation BGP Inc., Zhuozhou, Hebei, China

³Department of Geophysics and Information, College of Geoscience and Surveying Engineering, China University of Mining and Technology-Beijing, Beijing, China

⁴Jiangsu East China Geological Construction Group Co., Ltd., Nanjing, China

Abstract

Deep geothermal reservoirs are expected to serve as a sustainable resource for clean energy production, contributing to the achievement of global dual-carbon targets. This study analyzes the seismic acquisition method for soft-structure fracture zones in deep geothermal reservoirs through forward modeling analysis. Based on geological data from the Baoying area, China, a 2D geological model integrating formation velocities, densities, and stochastic fracture media within the Upper Sinian-Middle Ordovician strata—was constructed for the forward modeling. To enhance the accuracy of seismic simulations and reduce numerical dispersion, high-order finite-difference methods were employed. A detailed theoretical analysis of seismic dispersion characteristics indicates that higher-order spatial and temporal differences can effectively mitigate numerical dispersion. Numerical seismic forward simulations were performed using a 10th-order difference accuracy, with a detailed analysis of acquisition survey parameters such as trace spacing, shot spacing, maximum offset, and record length. Simulated records for the geological model with and without fracture zones were compared, revealing distinct differences, particularly when fracture zones are located within high-velocity layers. Further analysis of pre-stack depth migration profiles with varying offsets, trace spacings, and shot intervals indicates that a maximum offset above 7000 m, a trace spacing of 5 m (or 10 m as a cost-effective option), and a shot interval of 40 m provide optimal imaging accuracy for fracture zones. These findings offer guidance for improving seismic imaging and interpretation of soft structures within fracture zones, thereby enhancing seismic exploration of deep geothermal reservoirs.

Keywords: Deep geothermal reservoirs; Soft structures; Fracture zones; Forward modeling; High-order finite-difference; Seismic acquisition

*Corresponding authors:

Fei Gong (cupgongfei@163.com) Ping Che (cheping@foxmail.com)

Citation: Fu G, Tan Z, Men Z, et al. Forward modeling study of seismic acquisition for fractured soft structures in deep geothermal reservoirs. *J Seismic Explor*. 2025;34(3):61-75. doi: 10.36922/JSE025320054

Received: August 8, 2025
Revised: September 4, 2025
Accepted: September 16, 2025

Published online: October 13,

2025

Copyright: © 2025 Author(s). This is an Open-Access article distributed under the terms of the Creative Commons Attribution License, permitting distribution, and reproduction in any medium, provided the original work is properly cited.

Publisher's Note: AccScience Publishing remains neutral with regard to jurisdictional claims in published maps and institutional affiliations.

1. Introduction

The pursuit of sustainable energy sources has become a global imperative, driven by the need to mitigate climate change and reduce greenhouse gas emissions. Among various renewable energy options, geothermal energy stands out due to its potential to provide a reliable and carbon-neutral energy supply. Deep geothermal reservoirs are known to hold vast amounts of untapped geothermal energy; however, the exploration and exploitation of these resources are hindered by the complex geological structures in deeply buried environments.¹⁻⁴

Seismic exploration is a crucial technique for mapping and characterizing subsurface geological structures.⁵⁻⁸ It involves the generation and recording of seismic waves that are reflected or refracted by geological interfaces. The analysis of these seismic data provides insights into the subsurface geology, enabling the identification and assessment of potential geothermal reservoirs. For deep geothermal reservoirs, successful exploration and identification heavily rely on the capability to accurately image and interpret subsurface geological structures.9,10 However, deep geothermal reservoirs are often associated with soft-structure fracture zones containing fluids and gases, 11-14 which can significantly affect seismic wave propagation, leading to complex seismic responses that are difficult to interpret using conventional methods. In addition, the great depths of these reservoirs often result in weak seismic signals with low data quality. 15,16 Further hindering the efficiency of seismic acquisition. Although seismic forward modeling has been extensively studied in the context of oil and gas reservoirs, such analyses are rarely applied to deep geothermal reservoirs, and published research remains very limited. Therefore, there is a pressing need to develop advanced seismic acquisition and imaging techniques that can address the challenges posed by softstructure fracture zones in deep geothermal environments.

Previous studies have made significant contributions to understanding seismic wave propagation in complex geological structures.¹⁷⁻²⁰ In particular, various numerical modeling methods, such as finite-difference,²¹ finite-element,²² and spectral element²³ methods, have been developed to simulate seismic wave propagation through geological models. These studies have provided valuable insights into the effects of fractures on seismic wave propagation and have identified key factors influencing seismic responses in fractured media. For example, Lan *et al.*²⁴ presented a finite-difference-based simulation method for the elastic wave equation in fractured media with a non-flat free surface, highlighting the complexity of scattered waves induced by fractures and surface conditions. Ren *et al.*²⁵ proposed an implicit

staggered-grid finite-difference scheme with sampling-approximated optimal coefficients to improve numerical accuracy for seismic modeling of complex structures. However, most existing studies have focused on relatively simple fracture geometries and have not fully accounted for the stochastic nature of natural fractures. In addition, the impact of soft formations on seismic wave propagation has rarely been addressed, limiting the applicability of these findings to practical geothermal exploration.

In addition to the complexity of seismic modeling/ responses caused by the stochastic nature of fractures, the presence of soft formations can lead to significant attenuation and dispersion of seismic waves, 26,27 further complicating the seismic data acquisition. In seismic exploration, acquisition survey parameters, such as offset, trace spacing, and shot interval, greatly affect the seismic processing, imaging, and interpretation.²⁸⁻³¹ For example, Zhang³² proposed optimized sparse seismic acquisition designs combined with compressive sensing reconstruction, achieving high-quality seismic imaging using only 25% of the receivers. Tsingas et al.33 developed a novel 3D distributed blended seismic acquisition scheme, combined with advanced deblending algorithms that produced fullbandwidth seismic images. Zhao et al.34 presented an irregular seismic acquisition method combining curvelet transform and simulated annealing to optimize observation system design in complex areas. However, the analysis of optimal acquisition parameters for seismic surveys targeting fracture zones in deep geothermal reservoirs has not been systematically studied. There remains a lack of quantitative guidelines for selecting acquisition survey parameters in such complex geological settings.

To address the aforementioned issues, this study aims to fill these research gaps by employing forward modeling analysis to investigate the seismic acquisition method for soft-structure fracture zones in deep geothermal reservoirs. In this context, "soft structures" refer to lowvelocity, low-modulus, and relatively weakened fracture zones or fractured rock bodies filled with fluids and/ or gases within deep geothermal reservoirs. Compared to the surrounding host rock, these structures exhibit lower elastic moduli and higher attenuation and energy dissipation. By constructing a 2D geological model that incorporates stochastic fracture media and soft formations, and using high-order finite-difference methods to simulate seismic wave propagation, this study seeks to provide a more comprehensive understanding of seismic responses in complex geological environments. Furthermore, through the analysis of pre-stack depth migration (PSDM) profiles with varying acquisition parameters, this study aims to identify optimal seismic acquisition strategies for

imaging soft structures within fracture zones. Overall, this work presents an initial set of optimal acquisition survey parameters based on detailed seismic forward modeling analysis for deep geothermal reservoirs with complex fractures, thereby contributing to the advancement of geothermal exploration techniques.

2. Geological model

The geological model for this study is based on the geological profile from the Baoying area, Jiangsu province, an important geothermal exploration target in China. 35,36 The Baoying area provides detailed geological structure information on deep geothermal reservoirs, and a reference line is selected for seismic forward modeling (Figure 1A). Based on this reference line, the initial geological model was constructed for further analysis, as shown in Figure 1B. According to geophysical parameters from the area, interval velocities, densities, and other formation properties were assigned to the initial geological model.

To analyze the effects of fractures on seismic modeling and acquisition, three fracture structures with varying sizes and geometries were introduced into the geological model. The fracture zones are located within the Upper Sinian–Middle Ordovician strata (outlined by the blue polygonal area in Figure 1A), corresponding geologically to the location of deep geothermal reservoirs. Specifically, the interiors of these fracture zones are filled with stochastic fracture media using a random medium modeling approach. Figure 2A further displays the grid model incorporating the fracture zones, with a close-up view shown in Figure 2B (fractures indicated by arrows). The color legend in Figure 2 represents P-wave velocity.

3. Numerical analysis

3.1. Methodologies

Forward modeling simulates the seismic response of underground elastic models. Seismic propagation can be described by the acoustic wave equation, with the constant-density 2D form expressed as:³⁷

$$\frac{\partial^2 u}{\partial x^2} + \frac{\partial^2 u}{\partial z^2} = \frac{1}{V^2(x,z)} \frac{\partial^2 u}{\partial t^2}$$
 (I)

where u is the particle displacement, V is the particle velocity, t is the time, and x, z represent the Cartesian coordinates.

Finite-difference methods are commonly used to numerically solve the acoustic wave equation and simulate wave propagation.²¹ In particular, high-order finite-difference methods can enhance the accuracy of temporal differencing. To mitigate the excessive memory requirements of the algorithm, high-order time derivatives of the wavefield can be converted into high-order spatial derivatives.

For spatial differencing, the second-order derivative can be approximated using a $2M^{\text{th}}$ -order difference accuracy finite-difference scheme in the following form:

$$\frac{\partial^2 f}{\partial x^2} = \frac{1}{\Delta x^2} \sum_{m=1}^{M} C_m^{(M)} [f(x + m\Delta x) - 2f(x) + f(x - m\Delta x)]$$
(II)

where C_m is the m^{th} -order difference coefficient. Using a Taylor series expansion, these high-order coefficients can be obtained by solving the following system of equations:

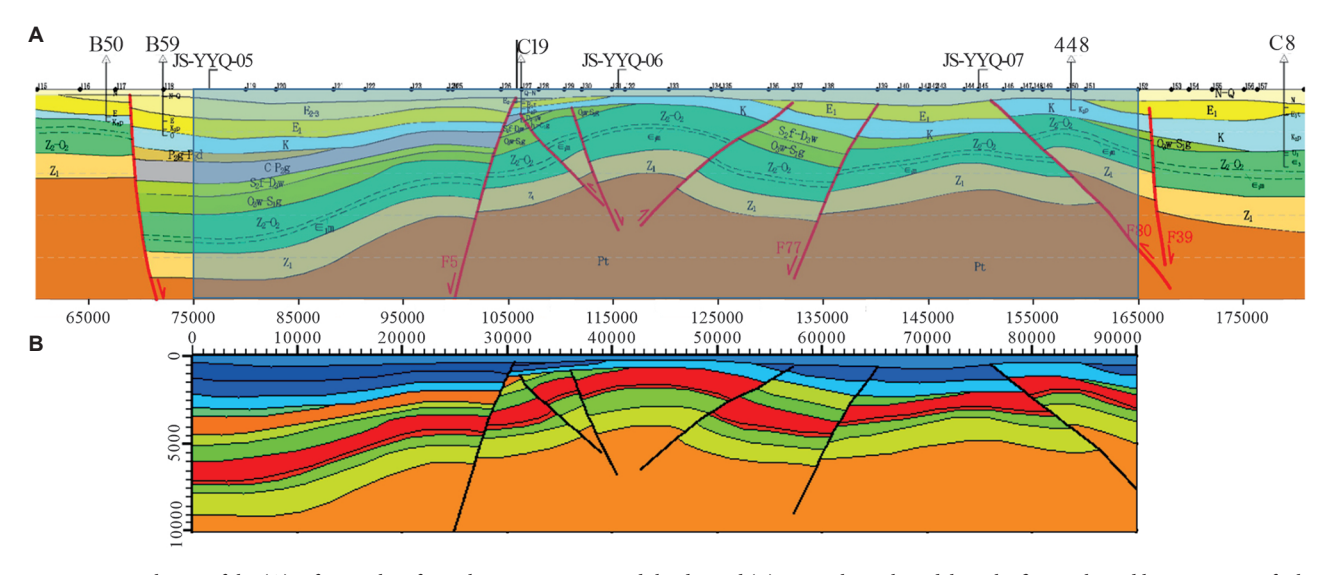


Figure 1. Partial view of the (A) reference line from the Baoying area, and the derived (B) 2D geological model. In the figure, the red lines represent faults, the black lines represent stratigraphic boundaries, and the dashed black lines represent unconformities.

Volume 34 Issue 3 (2025) 63 doi: 10.36922/JSE025320054

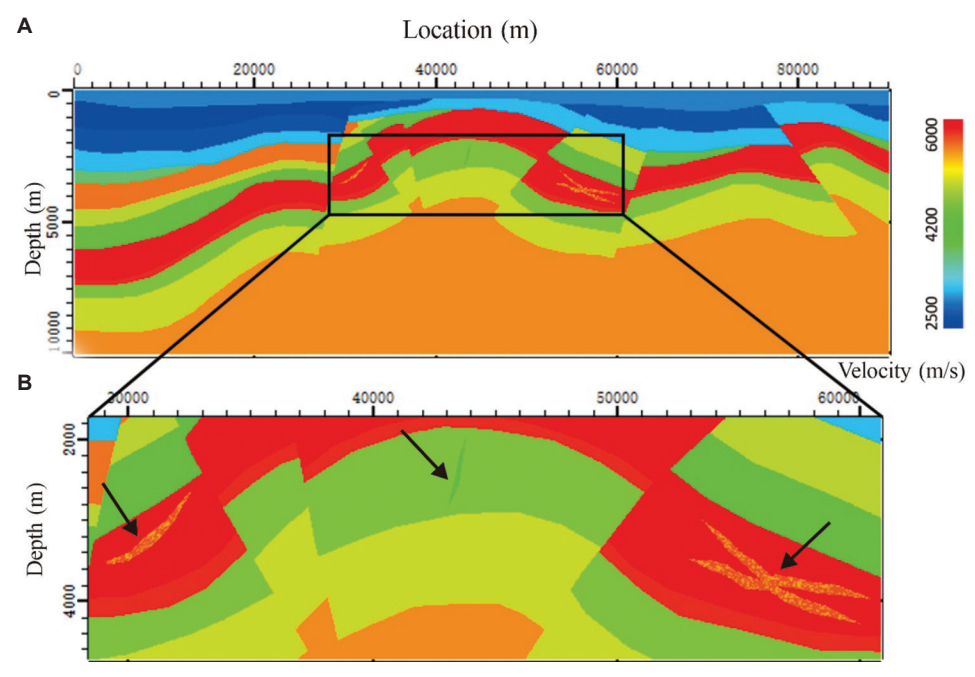


Figure 2. Geological model containing the fracture zones for the forward modeling. (A) Grid model incorporating fracture zone structures; (B) Close-up view of the grid model with fracture zone structures indicated by arrows.

$$\begin{bmatrix} 1^{2} & 2^{2} & 3^{2} & \cdots & M^{2} \\ 1^{4} & 2^{4} & 3^{4} & \cdots & M^{4} \\ 1^{6} & 2^{6} & 3^{6} & \cdots & M^{6} \\ \vdots & \vdots & \vdots & \ddots & \vdots \\ 1^{2M} & 2^{2M} & 3^{2M} & \cdots & M^{2M} \end{bmatrix} \begin{bmatrix} C_{1}^{(M)} \\ C_{2}^{(M)} \\ C_{3}^{(M)} \\ \vdots \\ C_{M}^{(M)} \end{bmatrix} = \begin{bmatrix} 1 \\ 0 \\ 0 \\ \vdots \\ 0 \end{bmatrix}$$
(III)

Numerical dispersion arises from grid discretization in numerical computations. It causes seismic waves of different frequencies to exhibit varying phase velocities, resulting in dispersion of seismic waves and reducing the effectiveness of numerical simulations and migration imaging. Although numerical dispersion is unavoidable in wave equations' solutions, its impact can be mitigated through methods that improve computational accuracy.

By applying the high-order differencing method described above, the accuracy of seismic wave numerical simulations can be improved and numerical dispersion reduced. This technique is crucial for enhancing the quality of simulation results. Accordingly, it enables the selection of appropriate simulation parameters in practical seismic modeling, thereby improving seismic imaging and interpretation of deep fracture zones. Given the significance of dispersion effects, a detailed analysis is presented in the following section to better understand both spatial and temporal aspects of numerical dispersion.

3.2. Spatial dispersion analysis

For spatial numerical dispersion, we examined the dispersion characteristics of the spatial $2N^{\text{th}}$ -order spatial difference accuracy approximation for the 2D wave equation. Assuming that the propagation direction of the plane wave forms an angle θ with the x-axis, substituting the plane harmonic wave $u(x,z,t) = \exp[i(wt-kx\cos\theta-kz\sin\theta)]$ into the $2N^{\text{th}}$ -order spatial difference formula (assuming that $\Delta z = \Delta x$):

$$\frac{1}{V_0^2} \frac{\partial^2 u}{\partial t^2} = \frac{1}{\Delta x^2} \sum_{n=1}^N C_n^{(N)} \left[u(x + n\Delta x, z) + u(x - n\Delta x, z) + u(x, z + n\Delta x) + u(x, z + n\Delta x) - 4u(x, z) \right]$$
(IV)

Based on **Equation IV**, we can further derive:

$$\frac{V}{V_0} = \sqrt{\frac{-2}{\phi^2} \{ \sum_{n=1}^{N} C_n^{(N)} [\cos(n\phi\cos\theta) + \cos(n\phi\sin\theta) - 2] \}}$$
 (V)

where $V = \omega/k$ is the phase velocity of the seismic wave, $\varphi = k\Delta x = 2\pi\Delta x/\lambda$ is the phase angle, and θ is the angle between the propagation direction and the coordinate axis.

Figure 3 displays the variation curves of spatial numerical dispersion for propagation angles $\theta = 0^{\circ}$, $\theta = 22.5^{\circ}$, and $\theta = 45^{\circ}$, under spatial difference accuracies of $2^{\rm nd}$, $4^{\rm th}$, $6^{\rm th}$, $8^{\rm th}$, and $10^{\rm th}$ orders, respectively, plotted as a function of the number of discrete points per wavelength.

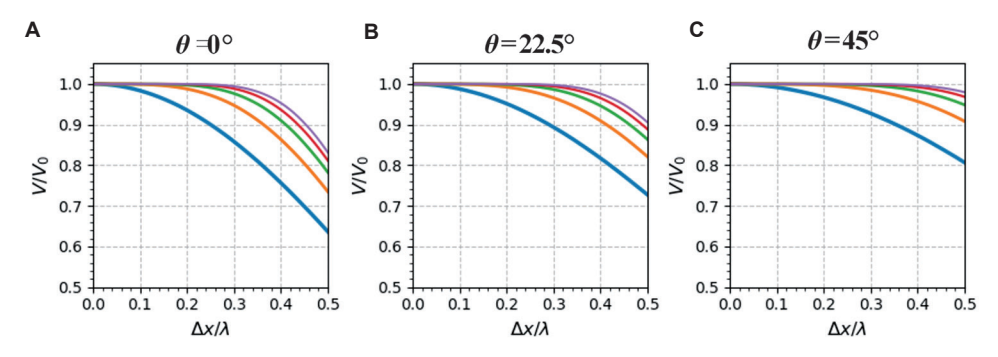


Figure 3. Numerical dispersion curves for wave propagation directions of (A) $\theta = 0^{\circ}$, (B) $\theta = 22.5^{\circ}$, and (C) $\theta = 45^{\circ}$, given varying spatial difference accuracies (2^{nd} , 4^{th} , 6^{th} , 8^{th} , and 10^{th} orders)

From Figure 3 and Equation V, it can be observed that numerical dispersion caused by spatial difference is determined by three factors: (i) The propagation direction of the seismic wave, (ii) the spatial difference accuracy, and (iii) the number of discrete points per wavelength (grid spacing). Their relationships with dispersion are presented below.

As the angle between the propagation direction and the discrete coordinate axis increases, the degree of numerical dispersion decreases. For a plane wave propagating at an angle θ to the *x*-axis, the spatial numerical dispersion is equivalent to that of a wave propagating at an angle of $90^{\circ} - \theta$. In other words, the discrete numerical dispersion is minimal when $\theta = 45^{\circ}$ (Figure 3C).

Regardless of the propagation direction, increasing the spatial difference accuracy order reduces the numerical dispersion. Therefore, there is a direct relationship between numerical dispersion and difference accuracy: Higher-order spatial differences effectively suppress dispersion. Unless the grid spacing is very fine (e.g., more than 15 spatially discrete points per wavelength, which implies low simulation efficiency), conventional second-order spatial differencing leads to severe dispersion. In contrast, higher-order methods, such as eighth- or 10th-order differencing, significantly improve accuracy, even when using only four grid points per wavelength. In general, adopting an eighth-order spatial difference accuracy is sufficient to suppress numerical dispersion.

For any order of spatial differencing, as the number of discrete points per wavelength increases (i.e., as grid spacing decreases), numerical dispersion is further reduced, and the accuracy of seismic wave simulation improves. This analysis confirms that numerical dispersion can be mitigated by employing high-order difference methods, and numerical simulation results validate this conclusion.

Figure 4 shows the single-shot simulation records for a single-interface model using second-order and 10^{th} -order spatial difference accuracies, with $\Delta x = \Delta z = 10$ m and

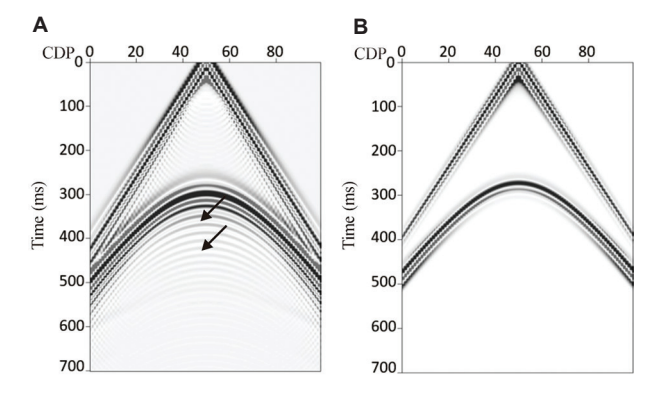


Figure 4. Numerical simulations for a single-interface model using (A) second-order and (B) 10th-order spatial difference accuracy Abbreviation: CDP: Common depth point

 $\Delta t = 1$ ms. It can be observed that numerical dispersion from second-order spatial differencing (Figure 4A) is severe, particularly for vertically propagating waves, while higher-order differencing effectively mitigates spatial dispersion.

In addition, Figure 4 demonstrates that $V < V_o$; that is, numerical dispersion caused by spatial discretization appears as a trailing waveform (indicated by arrows in Figure 4A). Given that $\varphi = 2\pi f \Delta x/V_o$, for a constant grid spacing, higher wavelet frequencies and lower medium velocities lead to more severe dispersion. Therefore, in cases involving lower-velocity media (such as low shearwave velocities), while high-frequency resolution is required, high-order differencing methods should be used to suppress numerical dispersion.

3.3. Temporal dispersion analysis

For the analysis of temporal numerical dispersion, we substitute the harmonic wave $u(x,z,t) = \exp[i(wt-kx\cos\theta-kz\sin\theta)]$ into the following equation:

$$\frac{\partial^{2} u}{\partial x^{2}} + \frac{\partial^{2} u}{\partial z^{2}} = \frac{1}{V_{0}^{2} \Delta t^{2}} \sum_{m=1}^{M} C_{m}^{(M)} \left[u(t + m\Delta t) - 2u(t) + u(t - m\Delta t) \right]$$
(VI)

Based on Equation VI, we can further derive:

$$\frac{V_0}{V} = \sqrt{\frac{-1}{2\pi^2} \frac{1}{\left(\frac{\Delta t}{T}\right)^2} \sum_{m=1}^{M} C_m^{(M)} \left[\cos(2m\pi \frac{\Delta t}{T}) - 1\right]}$$
(VII)

where $V = \omega/k$ is the phase velocity of the seismic wave, T is the period of the seismic wave, and Δt is the time step length.

Figure 5 displays the variation curves of temporal discrete numerical dispersion as a function of $\Delta t/T$, for different difference accuracies of $2^{\rm nd}$, $4^{\rm th}$, $6^{\rm th}$, $8^{\rm th}$, and $10^{\rm th}$ orders. It can be observed that: (i) when $V > V_{\rm o}$, numerical dispersion caused by temporal discretization appears as early arrivals in the waveform (i.e., before the actual arrival time), and (ii) as the difference accuracy 2M increases, the numerical dispersion introduced by the high-order differencing gradually decreases.

From **Equation VII**, it is evident that temporal numerical dispersion is primarily governed by two factors: (i) The difference in accuracy and (ii) the number of discrete points within 1 time period (also illustrated in Figure 5). Due to algorithmic stability constraints, $\Delta t/T$ is generally very small. As a result, numerical dispersion during the forward and reverse propagation of seismic waves is mainly attributed to spatial discretization rather than temporal discretization. To address temporal numerical dispersion, adopting the fourth-order temporal difference accuracy is generally sufficient. Higher-order temporal difference accuracies have minimal impact on mitigating numerical dispersion and may instead reduce simulation efficiency.

3.4. Stability analysis

Stability is a fundamental issue in numerically solving seismic wave equations. An unreasonable selection of discrete parameters during numerical computations may produce computed results that grow exponentially without physical meaning, resulting in severe numerical dispersion

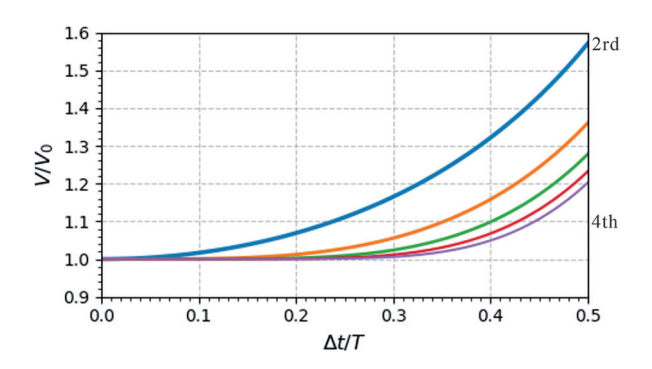


Figure 5. Numerical dispersion curves for varying temporal difference accuracies $(2^{nd}, 4^{th}, 6^{th}, 8^{th}, and 10^{th} orders)$

in simulation results. In extreme cases, this can lead to overflow errors and render computations unfeasible. Therefore, for any numerical solution method, it is necessary to determine the range of discrete parameters that ensure computational stability, i.e., to assess the method's stability. In this study, we analyzed the stability of the high-order finite-difference method for the 2D acoustic wave equation and provided corresponding stability conditions for various difference accuracies.

The difference scheme for the $2N^{\text{th}}$ -order spatial difference accuracy of the 2D acoustic wave equation can be written as:

$$u(t + \Delta t) \approx 2u(t) - u(t - \Delta t)$$

$$+V^{2} \Delta t^{2} \left\{ \frac{1}{\Delta x^{2}} \sum_{n=1}^{N} C_{n}^{(N)} \left[u(x + n\Delta x) - 2u(x) + u(x - n\Delta x) \right] \right\}$$

$$+V^{2} \Delta t^{2} \left\{ \frac{1}{\Delta z^{2}} \sum_{n=1}^{N} C_{n}^{(N)} \left[u(z + n\Delta z) - 2u(z) + u(z - n\Delta z) \right] \right\}$$
(VIII)

Applying a Fourier transform to both sides of **Equation VIII** with respect to time and space yields:

$$\cos(\omega \Delta t) - 1 \approx V^2 \Delta t^2 \left\{ \frac{1}{\Delta x^2} \sum_{n=1}^{N} C_n^{(N)} \left[\cos(\hat{k}_x n \Delta x) - 1 \right] \right\}$$
$$+ V^2 \Delta t^2 \left\{ \frac{1}{\Delta z^2} \sum_{n=1}^{N} C_n^{(N)} \left[\cos(\hat{k}_z n \Delta z) - 1 \right] \right\}$$
(IX)

where k is the wavenumber and w is the angular frequency. To satisfy **Equation IX**, the following condition must be satisfied:

$$-2 \le V^{2} \Delta t^{2} \left\{ \frac{1}{\Delta x^{2}} \sum_{n=1}^{N} C_{n}^{(N)} \left[\cos(\hat{k}_{x} n \Delta x) - 1 \right] + \left\{ \frac{1}{\Delta z^{2}} \sum_{n=1}^{N} C_{n}^{(N)} \left[\cos(\hat{k}_{z} n \Delta z) - 1 \right] \right\} \le 0$$
 (X)

Given that the spatial difference coefficients C_n alternate between positive and negative values, the maximum spatial wavenumber is the Nyquist wavenumber $k = \pi/\Delta x$. Therefore, the stability condition for the $2N^{\text{th}}$ -order spatial difference accuracy of the 2D acoustic wave equation is given by:

$$0 \le V^2 \Delta t^2 \left(\frac{1}{\Delta x^2} + \frac{1}{\Delta z^2} \right) \sum_{n=1}^{N} C_n^{(N)} \left[1 - (-1)^n \right] \le 2$$
 (XI)

Equation XI can be further simplified to:

$$V\Delta t \sqrt{\frac{1}{\Delta x^2} + \frac{1}{\Delta z^2}} \le \sqrt{\frac{2}{\sum_{n=1}^{N} C_n^{(N)} \left[1 - (-1)^n\right]}}$$
 (XII)

Equation XII serves as a general stability criterion for high-order finite-difference methods in acoustic wave simulations with varying difference accuracies. Based on different values of *N*, stability conditions for different orders of spatial difference accuracy are listed in Table 1. The results indicate that as the spatial difference accuracy increases, the stability requirements for high-order grid-based methods increase slightly. However, the increase is relatively modest. In other words, discrete grid parameters that satisfy the stability conditions for lower-order schemes generally meet

Table 1. Stability conditions for different orders of spatial difference accuracy

Orders N of spatial difference $(\Delta x = \Delta z)$	Stability condition	
	$V\Delta t\sqrt{\frac{1}{\Delta x^2} + \frac{1}{\Delta z^2}}$	$\frac{V\Delta t}{\Delta x}$
N=1	<1	<0.707
N=2	<0.866	< 0.612
N=3	< 0.813	< 0.575
N=4	< 0.784	< 0.555
<i>N</i> =5	<0.765	<0.541

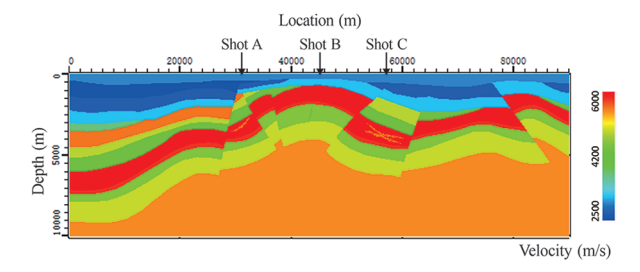


Figure 6. Illustration of the locations of shots A, B, and C on the geological model

the requirements for higher-order schemes. Thus, adopting high-order differencing does not impose significantly stricter demands on the choice of discrete parameters.

4. Simulation results

4.1. Single-shot record results

Based on the previous numerical analysis, seismic modeling was performed using the 10th-order finitedifference scheme applied to the 2D acoustic wave equation. In practice, an absorbing boundary condition³⁸ is employed to mitigate the effects of reflections from artificial boundaries. The geological model shown in Figure 1 was used, with an absorbing surface boundary condition applied at the surface. A Ricker wavelet with a dominant frequency of 40 Hz was utilized in the simulations. For the seismic acquisition survey, the trace spacing was set to 5 m, the shot spacing to 40 m, the maximum offset to 8000 m, and the minimum offset to 5 m. All single-shot records were captured for 8 s with a sampling interval of 2 ms. For comparison, single-shot records (Shots A, B, and C) were generated at different locations above the fracture zones, as illustrated in Figure 6.

Figures 7A, 8A, and 9A display the simulated shot records for shots A, B, and C with the fracture zones included in the model. Corresponding records without the fracture zones are shown in Figures 7B, 8B, and 9B, and the residuals (i.e., the differences between records with and without fracture zones) are depicted in Figures 7C, 8C, and 9C. The comparison and analysis reveal the following: (i) For shots A and C, where the fracture zones are located within high-velocity layers, the overlying strata exert minimal influence. Consequently, distinct differences in the shot records are observable (Figures 7C and 9C). (ii) For shot B, where the fracture zones are developed

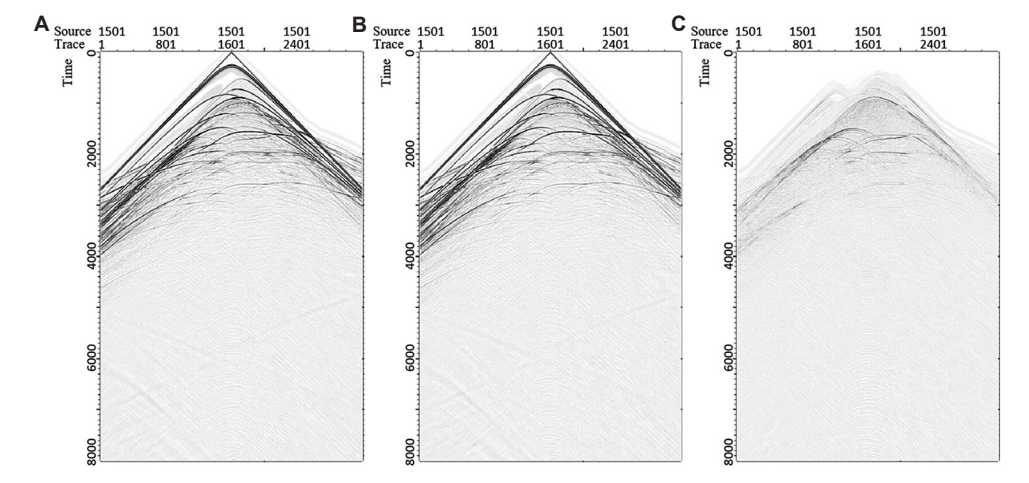


Figure 7. Simulated shot record (A) with fracture zones, (B) without fracture zones, and (C) residual difference between (A) and (B) for shot A

within low-velocity layers, the overlying strata significantly mask the effects of the fracture zones. As a result, no clear differences are visible in the residual record (Figure 8C).

4.2. Migration results

Based on the shot records, we further analyzed the PSDM^{39,40} results using different acquisition survey parameters. The PSDM was performed using the acoustic wave equation with the Fourier finite-difference method. For comparison, we evaluated the PSDM results by varying acquisition parameters, including maximum offset, trace spacing, and shot interval.

Figures 10-13 display the PSDM findings for maximum offsets of 8000 m, 7000 m, 6000 m, and 5000 m, respectively. Comparing these imaging results reveals that the migration with a 6000 m offset exhibits slightly lower accuracy for fracture imaging than those with 7000 m or larger offsets, showing poorer continuity of fracture structure and slightly

reduced resolution. The differences between the 7000 m and 8000 m offset migration results are negligible, as both offer nearly identical imaging accuracy. In contrast, the 5000 m offset produces significantly lower imaging quality. This analysis suggests that a maximum offset >7000 m is preferable for effectively revealing deep fracture zones.

Figures 14-17 exhibit the PSDM results with trace spacings of 5 m, 10 m, 20 m, and 40 m, respectively. Comparing these findings indicates that imaging accuracy for steeply dipping structures is significantly better with 5 m and 10 m trace spacings than with 20 m and 40 m spacings. While the overall disparity between 5 m and 10 m spacings is not substantial, the finer spatial sampling of 5 m produces clearer and more accurate imaging of fracture structures (as indicated by the arrows in Figure 14). Based on this analysis, 5 m trace spacing is recommended; however, if computational cost is a concern, a 10 m trace spacing may also be acceptable.

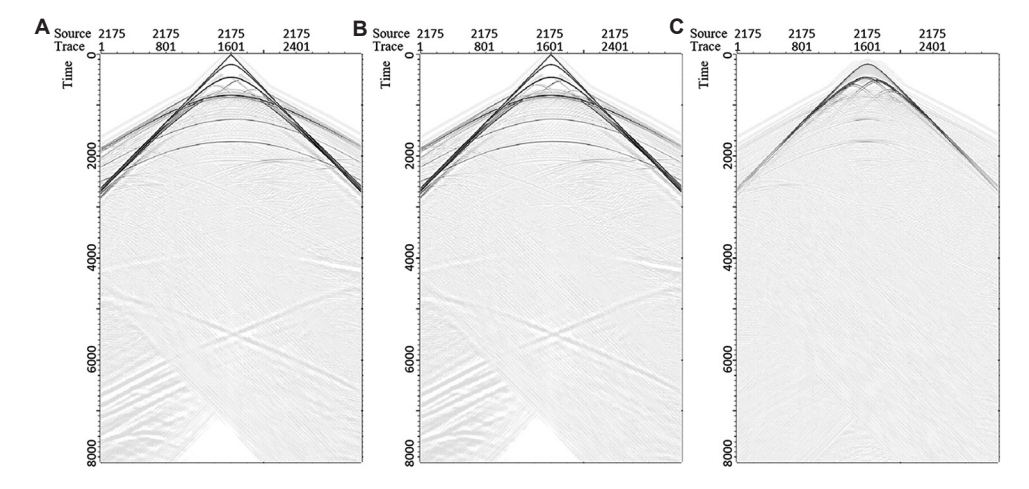


Figure 8. Simulated shot record (A) with fracture zones, (B) without fracture zones, and (C) residual difference between (A) and (B) for shot B

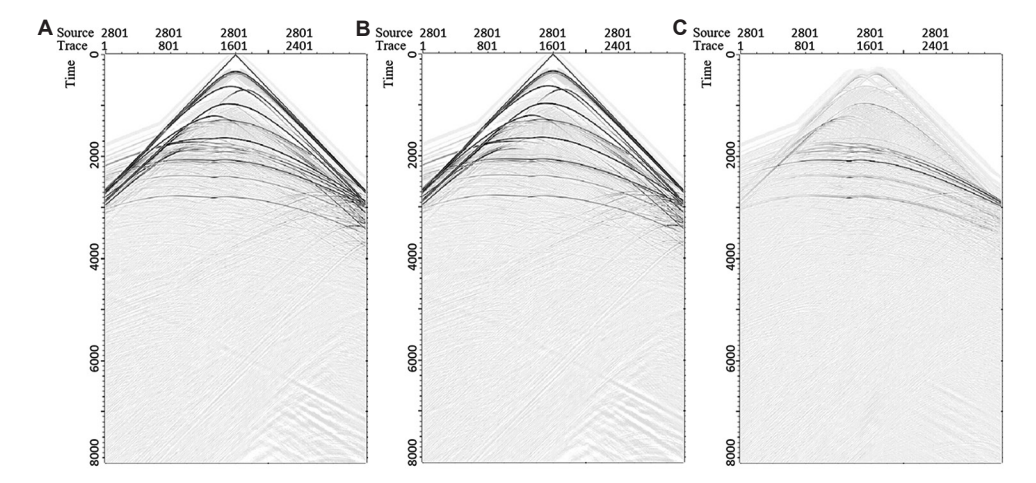


Figure 9. Simulated shot record (A) with fracture zones, (B) without fracture zones, and (C) residual difference between (A) and (B) for shot C

Volume 34 Issue 3 (2025) 68 doi: 10.36922/JSE025320054

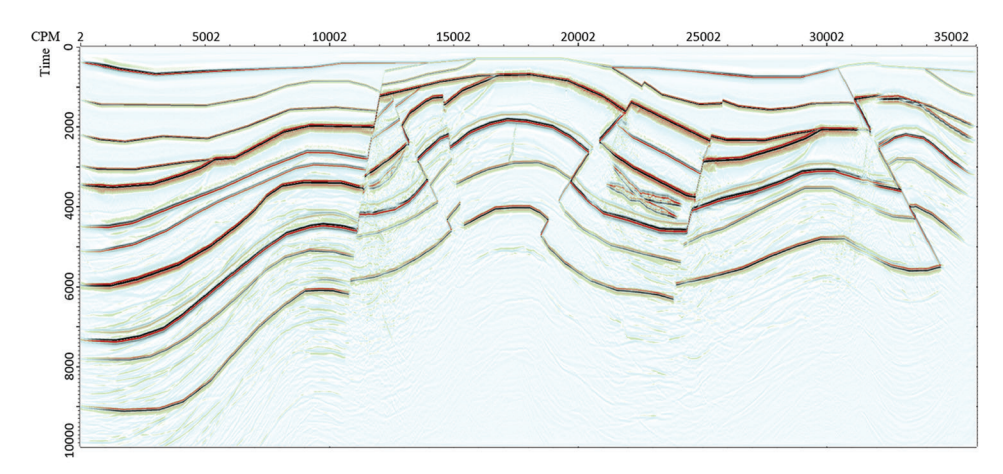


Figure 10. Pre-stack depth migration result with maximum offset of 8000 m (bin size: 2.5 m; fold: 200) Abbreviation: CPM: Common middle point.

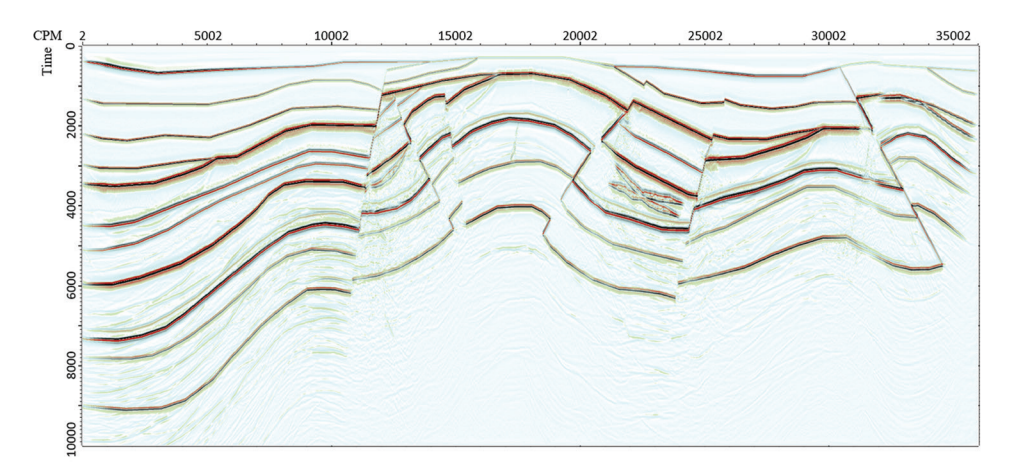


Figure 11. Pre-stack depth migration result with a maximum offset of 7000 m (bin size: 2.5 m; fold: 175) Abbreviation: CPM: Common middle point.

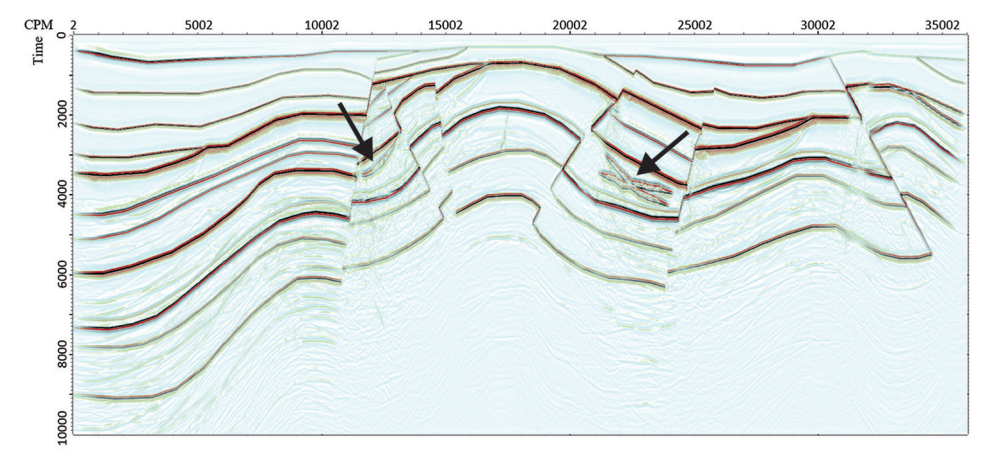


Figure 12. Pre-stack depth migration result with a maximum offset of 6000 m (bin size: 2.5 m; fold: 150) Abbreviation: CPM: Common middle point.

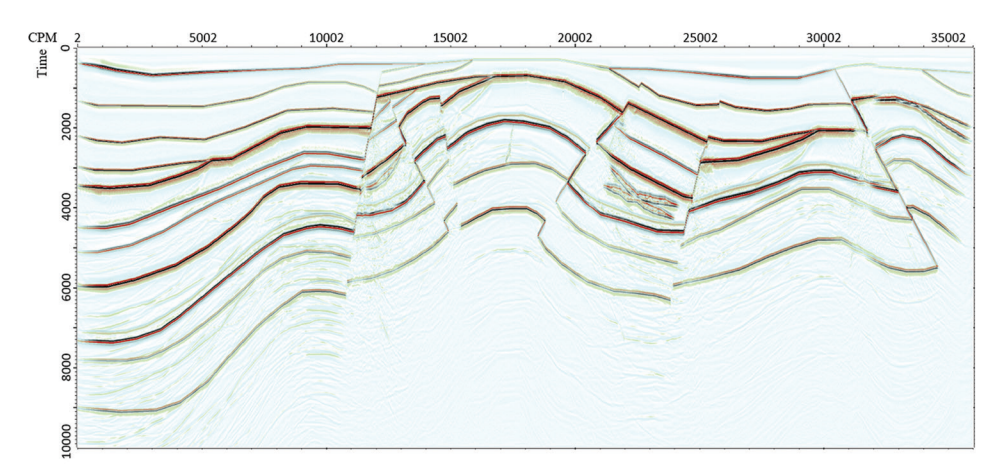


Figure 13. Pre-stack depth migration result with a maximum offset of 5000 m (bin size: 2.5 m; fold: 150) Abbreviation: CPM: Common middle point.

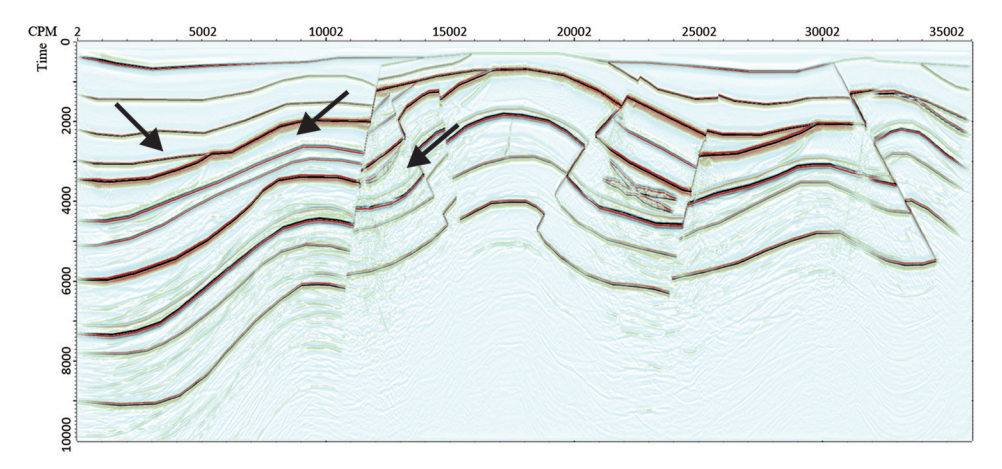


Figure 14. Pre-stack depth migration result with trace spacing of 5 m (bin size: 2.5 m; fold: 200) Abbreviation: CPM: Common middle point.

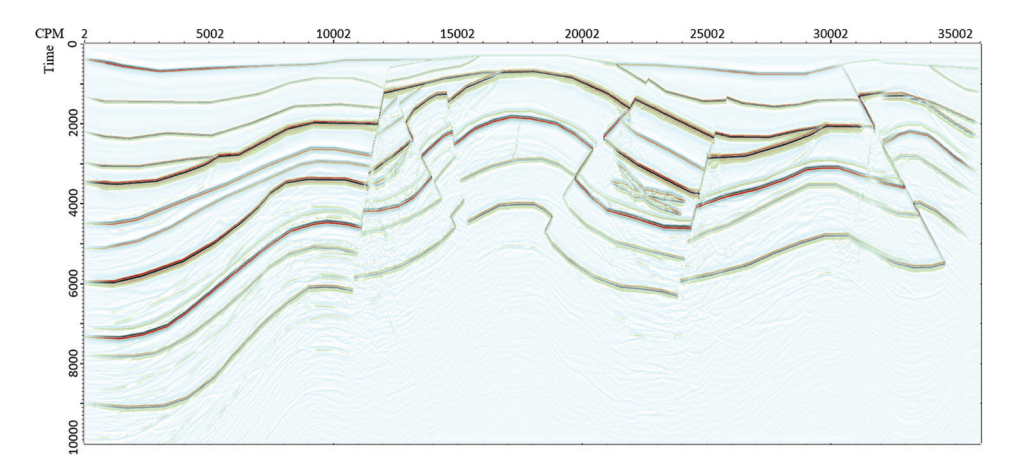


Figure 15. Pre-stack depth migration result with trace spacing of $10~\mathrm{m}$ (bin size: $5~\mathrm{m}$; fold: 200) Abbreviation: CPM: Common middle point.

Volume 34 Issue 3 (2025) 70 doi: 10.36922/JSE025320054

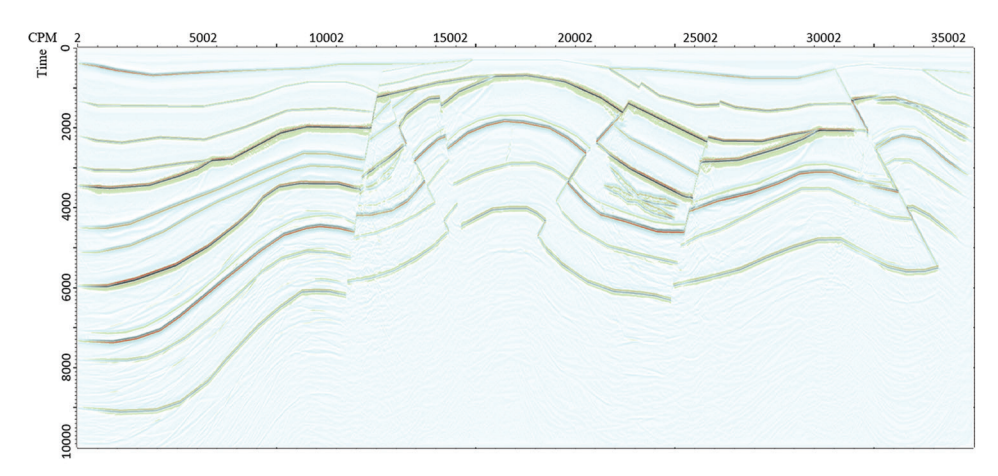
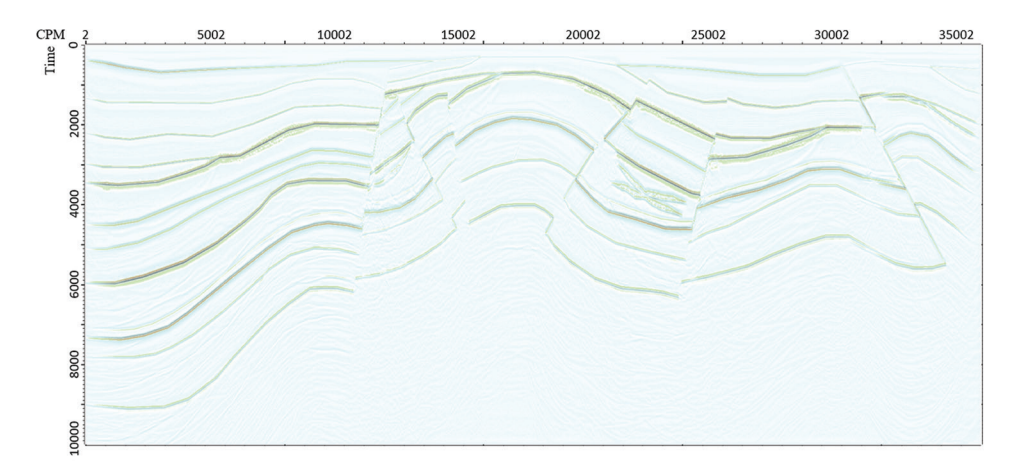


Figure 16. Pre-stack depth migration result with trace spacing of 20 m (bin size: 10 m; fold: 200) Abbreviation: CPM: Common middle point.



 $\textbf{Figure 17.} \ Pre-stack \ depth \ migration \ result \ with \ trace \ spacing \ of 40 \ m \ (bin \ size: 20 \ m; fold: 200) \ Abbreviation: \ CPM: \ Common \ middle \ point.$

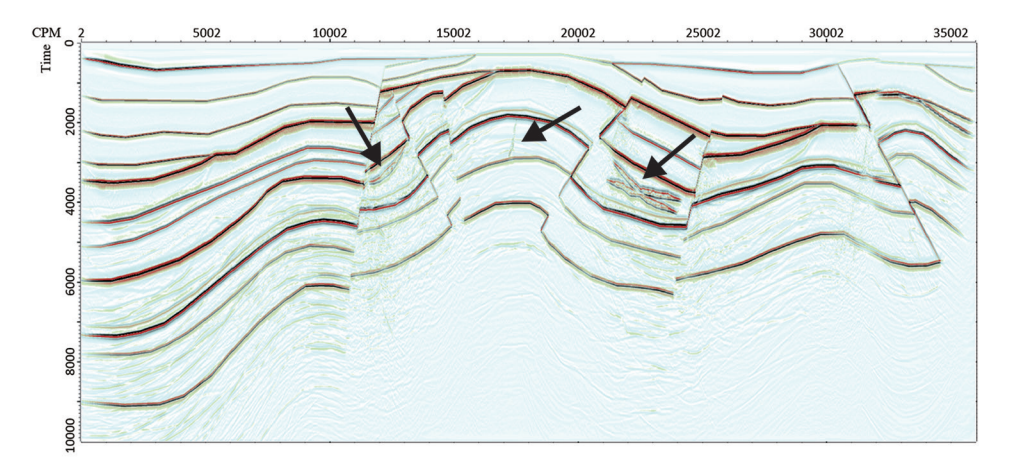


Figure 18. Pre-stack depth migration result with a maximum shot interval of 40 m (bin size: 2.5 m; fold: 200) Abbreviation: CPM: Common middle point.

Volume 34 Issue 3 (2025) 71 doi: 10.36922/JSE025320054

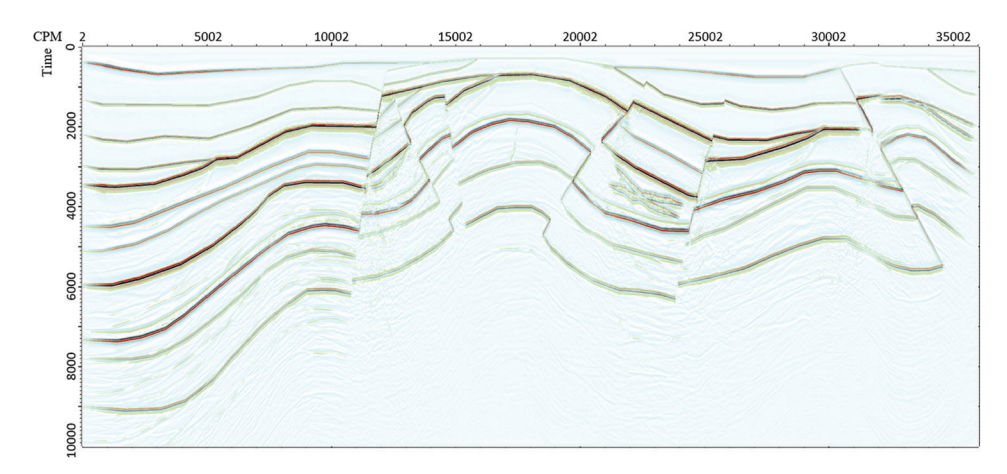


Figure 19. Pre-stack depth migration result with a maximum shot interval of 80 m (bin size: 2.5 m; fold: 100) Abbreviation: CPM: Common middle point.

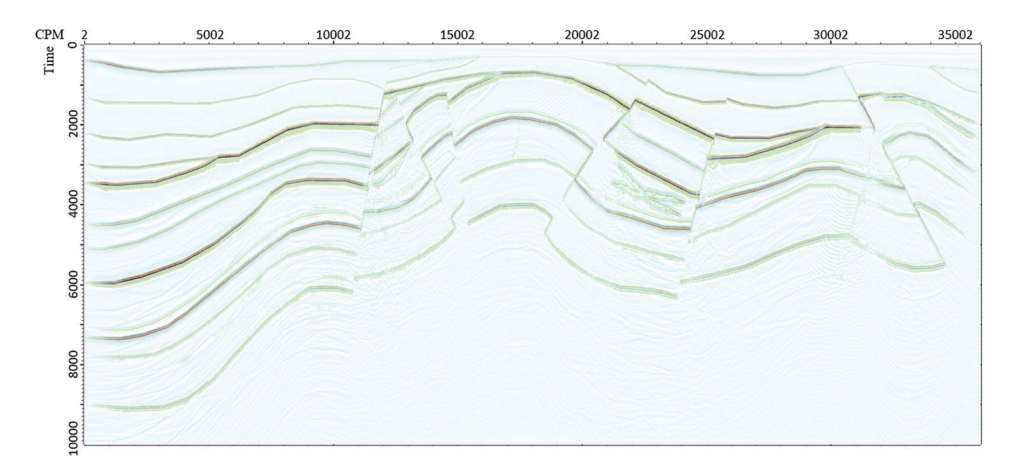


Figure 20. Pre-stack depth migration result with a maximum shot interval of 160 m (bin size: 2.5 m; fold: 50) Abbreviation: CPM: Common middle point.

Figures 18-20 display the PSDM results for shot intervals of 40 m, 80 m, and 160 m, respectively. Comparing these outcomes demonstrates that the 40 m shot interval provides a clear advantage in imaging fracture zones (indicated by the arrows in Figure 18).

5. Discussion

This study focuses on forward modeling analysis to investigate seismic acquisition strategies for soft-structure fracture zones within deep geothermal reservoirs. However, the analysis in this study is primarily based on numerical simulations and does not yet incorporate measured observational data. Although the geological model was constructed to closely reflect actual geological conditions, discrepancies may still exist between the simulation results and real seismic observations. Such discrepancies could arise from geological complexities, uncertainties in seismic wave propagation, and noise interference in real-world data.

In further studies, we aim to implement more advanced wavefield numerical simulation techniques, such as full waveform modeling and spectral element methods, to enhance the accuracy of seismic forward modeling.

Furthermore, this work centers on the influence of acquisition survey parameters (e.g., maximum offset, trace spacing, and shot interval) on seismic migration results, without evaluating the impact of different migration techniques, which can significantly affect imaging quality. Various migration approaches (e.g., Kirchhoff migration and reverse-time migration) may offer differing levels of effectiveness when applied to complex geological structures, including fracture zones. Therefore, the absence of comparative analysis on migration methods may limit our ability to fully interpret seismic imaging results. In future research, we plan to examine the performance of different migration techniques and their effects on fracture imaging in complex geological conditions.

In addition, the presence of fracture networks in softstructure zones introduces challenges such as seismic attenuation and anisotropy, both of which directly impact data quality and interpretability. Attenuation, primarily caused by scattering losses from stochastic fractures and fluid-induced viscoelastic dissipation, can reduce high-frequency content, particularly when fractures are hosted within high-velocity layers, necessitating finer bin sizes to maintain resolution. Meanwhile, fractureinduced anisotropy may require acquisition designs with multi-azimuth coverage and long offsets to capture anisotropy signatures. While the proposed acquisition parameters (40 m shot interval and 5 m bin size) strike a balance between cost and imaging accuracy, they should be complemented by anisotropic velocity modeling to optimize target illumination, an aspect warranting further investigation.

6. Conclusion

This study investigates the seismic acquisition design for soft-structure fracture zones within deep geothermal reservoirs through forward modeling analysis. By constructing a detailed 2D elastic model incorporating stochastic fracture media, based on the geological profile from the Baoying area of China, we successfully simulated seismic wave propagation with high fidelity. High-order finite-difference methods were employed to mitigate spatial and temporal numerical dispersion, enhancing the accuracy of seismic wave simulations. The comparison between simulated records with and without fracture zones revealed significant differences, particularly when the fractures were located within high-velocity layers. Further analysis of pre-stack depth migration profiles indicated that a maximum offset exceeding 7000 m, a trace spacing (bin size) of 5 m (or 10 m as a cost-effective alternative), and a shot interval of 40 m can provide optimal imaging accuracy for fracture zones. These findings are crucial for improving seismic imaging and interpretation of soft structures within fracture zones, thus enhancing the seismic exploration of deep geothermal reservoirs. Overall, this work provides quantitative guidelines for selecting seismic simulation and acquisition parameters in geothermal exploration under complex geological settings.

Acknowledgments

None.

Funding

This study was funded by the Jiangsu Province Carbon Peak Neutral Technology Innovation Project in China (BE2022034).

Conflict of interest

The authors declare no conflicts of interest.

Author contributions

Conceptualization: Guoqiang Fu, Zhe Men, Fei Gong, Ping Che

Formal analysis: Zhiyu Tan, Qiang Guo
Investigation: Zhe Men, Ping Che
Methodology: Guoqiang Fu, Fei Gong
Writing-original draft: Guoqiang Fu, Qiang Guo
Writing-review & editing: Zhiyu Tan, Xiaoge Wu, Fan
Xiao, Jingvi Lei

Availability of data

Data are not available due to restrictions related to the confidentiality of the project.

References

 Chopra S, Sharma RK., Bredesen K, Ha T, Marfurt KJ. Seismic characterization of a Triassic-Jurassic deep geothermal sandstone reservoir, onshore Denmark, using unsupervised machine learning techniques. *Interpretation*. 2021;9(4):T1097-T1106.

doi: 10.1190/INT-2021-0091.1

2. He K, Huang R, Xu Y, Hu S, Wei P. Crustal structures beneath the Northern Jiangsu Basin and its surrounding areas: Implications for geothermal prospecting. *J Geophys Eng.* 2022;19(3):316-325.

doi: 10.1093/jge/gxac018

3. Tian B, Lei X, Jiang H, Xu C, Song M. Multi-method geophysical mapping of a geothermal reservoir and buried channel in langfang, northern part of china. *J Environ Eng Geophys.* 2022;27(1):1-11.

doi: 10.32389/jeeg20-068

4. Wang X, Wang G, Gan H, Zhang Y, Gao Z. Constraints of hydrochemical and geological controls in deep-circulation geothermal systems: Insights from Chengde, Dehua, and Tashkorgan geothermal fields in China. *Geothermics*. 2025;127:103265.

doi: 10.1016/j.geothermics.2025.103265

5. Aleardi M, Mazzotti A. A feasibility study on the expected seismic AVA signatures of deep fractured geothermal reservoirs in an intrusive basement. *J Geophys Eng.*2014;11(6):065008.

doi: 10.1088/1742-2132/11/6/065008

 Dyer BC, Schanz U, Ladner F, Häring MO, Spillman T. Microseismic imaging of a geothermal reservoir stimulation. *Leading Edge*. 2008;27(7):856-869.

doi: 10.1190/1.2954024

7. Bredesen K, Dalgaard E, Mathiesen A, Rasmussen R, Balling N. Seismic characterization of geothermal sedimentary reservoirs: A field example from the Copenhagen area, Denmark. *Interpretation*. 2020;8(2):T275-T291.

doi: 10.1190/INT-2019-0184.1

8. Fu G, Peng S, Wang R, *et al.* Seismic prediction and evaluation techniques for hot dry rock exploration and development. *J Geophys Eng.* 2022;19(4):694-705.

doi: 10.1093/jge/gxac042

9. Samrock F, Grayver A, Dambly MLT, Müller MR, Saar MO. Geophysically guided well siting at the Aluto-Langano geothermal reservoir. *Geophysics*. 2023;88(5):WB105-WB114.

doi: 10.1190/geo2022-0617.1

10. Zheng, Y., Wang, Y. High-resolution reflection seismic imaging to reveal subsurface geologic structures of a deep geothermal reservoir. *Geophysics*. 2023;88(5):WB37-WB43.

doi: 10.1190/geo2022-0494.1

11. Darisma D, Mukuhira Y, Okamoto K, *et al.* Building the fracture network model for the Okuaizu geothermal field based on microseismic data analysis. *Earth Planets Space*. 2024;76(1):107.

doi: 10.1186/s40623-024-02049-w

12. Tian A, Fu G, Tang J, Wang D. Numerical simulation of the transport and sealing law of temporary plugging particles in complex fractures of carbonate-type thermal storage. *Energies*. 2024;17(13):3283.

doi: 10.3390/en17133283

13. Aydın H, Camcı U, Akın S. An experimental investigation of hydraulic fracturing mechanisms in menderes metamorphic rocks: Prospects for enhanced geothermal systems. *Geothermics*. 2025;130:103328.

doi: 10.1016/j.geothermics.2025.103328

14. Mu S, Zhao L, Zhang A. Numerical simulation of geothermal extraction for interaction between irregular curve fractures and heterogeneous reservoirs. *Rock Mech Rock Eng.* 2025;58(3):2953-2970.

doi: 10.1007/s00603-024-04339-x

15. Civilini F, Pancha A, Savage MK, Sewell S, Townend J. Inferring shear-velocity structure of the upper 200 m using cultural ambient noise at the Ngatamariki geothermal field, Central North Island, New Zealand. *Interpretation*. 2016;4(3):SJ87-SJ101.

doi: 10.1190/int-2015-0204.1

16. Nakata N, Bi Z, Qiu H, Liu CN, Nakata R. ML-aided induced seismicity processing and interpretation for enhanced geothermal systems. *Leading Edge*. 2025;44(4):265-275.

doi: 10.1190/tle44040265.1

17. Jianfeng Z, Tielin L. Elastic wave modelling in 3D heterogeneous media: 3D grid method. *Geophys J Int.* 2002;150(3):780-799.

doi: 10.1046/j.1365-246X.2002.01743.x

 Vlastos S, Liu E, Main IG, Li XY. Numerical simulation of wave propagation in media with discrete distributions of fractures: Effects of fracture sizes and spatial distributions. *Geophys J Int.* 2003;152(3):649-668.

doi: 10.1046/j.1365-246X.2003.01876.x

19. Hoffman BT, Chang WM. Modeling hydraulic fractures in finite difference simulators: Application to tight gas sands in Montana. *J Pet Sci Eng.* 2009;69(1-2):107-116.

doi: 10.1016/j.petrol.2009.08.007

 Yang D, Song G, Hua B, Calandra H. Simulation of acoustic wavefields in heterogeneous media: A robust method for automatic suppression of numerical dispersion. *Geophysics*. 2010;75(3):T99-T110.

doi: 10.1190/1.3428483

 Liu Y, Sen MK. An implicit staggered-grid finitedifference method for seismic modelling. *Geophys J Int.* 2009;179(1):459-474.

doi: 10.1111/j.1365-246X.2009.04305.x

22. Virieux J, Calandra H, Plessix R. A review of the spectral, pseudo-spectral, finite-difference and finite-element modelling techniques for geophysical imaging. *Geophys Prospect*. 2011;59(5):794-813.

doi: 10.1111/j.1365-2478.2011.00967.x

23. Hedayatrasa S, Bui TQ, Zhang C, Lim CW. Numerical modeling of wave propagation in functionally graded materials using time-domain spectral Chebyshev elements. *J Comput Phys.* 2014;258:381-404.

doi: 10.1016/j.jcp.2013.10.037

 Lan HQ, Zhang ZJ. Seismic wavefield modeling in media with fluid-filled fractures and surface topography. Appl Geophys. 2012;9(3):301-312.

doi: 10.1007/s11770-012-0341-5

25. Ren ZM, Dai X, Bao QZ. Source wavefield reconstruction based on an implicit staggered-grid finite-difference operator for seismic imaging. *Pet Sci.* 2022;19(5):2095-2106.

doi: 10.1016/j.petsci.2022.05.008

26. Carcione JM. Seismic modeling in viscoelastic media. *Geophysics*. 1993;58(1):110-120.

doi: 10.1190/1.1443340

27. Wang Y, Zhao L, Quintal B, Geng J. Characterizing broadband seismic dispersion and attenuation in carbonates with fractures and cavities: A numerical approach. *Geophys J Int.* 2025;240(3):1404-1425.

doi: 10.1093/gji/ggae452

28. Volker AWF, Blacquière G, Berkhout AJ, Ongkiehong L. Comprehensive assessment of seismic acquisition geometries by focal beams-Part II: Practical aspects and examples. *Geophysics*. 2001;66(3):918-931.

doi: 10.1190/1.1444982

29. Strong S, Hearn S. Multi-component seismic-resolution analysis using finite-difference acquisition modelling. *Explor Geophys.* 2008;39(4):189-197.

doi: 10.1071/EG08023

 Lubrano, Lavadera P, Kühn D, et al. CO₂ storage in the high Arctic: Efficient modelling of pre-stack depth-migrated seismic sections for survey planning. Geophys Prospect. 2018;66(6):1180-1200.

doi: 10.1111/1365-2478.12637

31. Ishiyama T, Blacquière G. 3-D shallow-water seismic survey evaluation and design using the focal-beam method: A case study offshore Abu Dhabi. *Geophys Prospect*. 2016;64(5):1215-1234.

doi: 10.1111/1365-2478.12335

- 32. Zhang M. Efficient 3D seismic acquisition design using compressive sensing principles. *J Seismic Explor*. 2023;32(5):427-454.
- Tsingas C, Almubarak MS, Jeong W, Al Shuhail A, Trzesniowski Z. 3D distributed and dispersed source array acquisition and data processing. *Leading Edge*. 2020;39(6):392-400.

doi: 10.1190/tle39060392.1

34. Zhao H, Chen MY, Ni YD, et al. Research on optimization method for irregular seismic acquisition in curved wave

domain based on simulated annealing. *Appl Geophys*. 2025;22(1):220-230.

doi: 10.1007/s11770-025-1181-4

- 35. Wang Y, Wang L, Hu D, *et al*. The present-day geothermal regime of the North Jiangsu basin, east china. *Geothermics*. 2020;88:101829.
 - doi: 10.1016/j.geothermics.2020.101829
- Zhang L, Li S, Xu W, et al. Discussion on deep geothermal characteristics and exploration prospects in the Northern jiangsu basin. Energies. 2024;17(13):3128.

doi: 10.3390/en17133128

 Yang L, Yan H, Liu H. Optimal implicit staggered-grid finitedifference schemes based on the sampling approximation method for seismic modelling. *Geophys Prospect*. 2016;64(3):595-610.

doi: 10.1111/1365-2478.12325

 Peng C, Toksöz MN. An optimal absorbing boundary condition for elastic wave modeling. *Geophysics*. 1995;60(1):296-301.

doi: 10.1190/1.1443758

- Shin C, Jang S, Min D. Improved amplitude preservation for prestack depth migration by inverse scattering theory. *Geophys Prospect.* 2001;49(5):592-606.
 - doi: 10.1046/j.1365-2478.2001.00279.x
- Zhou H, Lin H, Sheng SB, Chen HM, Wang Y. High angle prestack depth migration with absorption compensation. *Appl Geophys.* 2012;9(3):293-300.

doi: 10.1007/s11770-012-0339-z